Three-dimensional bioprinting of multicell-laden scaffolds containing bone morphogenic protein-4 for promoting M2 macrophage polarization and accelerating bone defect repair in diabetes mellitus

Xin Sun[a,1], Zhenjiang Ma[a,1], Xue Zhao[b,c,1], Wenjie Jin[a], Chenyu Zhang[a], Jie Ma[a], Lei Qiang[a,d], Wenhao Wang[a,d], Qian Deng[a,d], Han Yang[e], Jinzhong Zhao[f], Qianqian Liang[g], Xiaojun Zhou[h,***], Tao Li[i,**], Jinwu Wang[a,*]

[a] Shanghai Key Laboratory of Orthopaedic Implants, Department of Orthopaedic Surgery, Shanghai Ninth People's Hospital, Shanghai JiaoTong University School of Medicine, No. 639 Zhizaoju Road, Shanghai, 200011, China
[b] Department of Radiology, Shanghai Ninth People's Hospital, Shanghai JiaoTong University School of Medicine, No. 639 Zhizaoju Road, Shanghai, 200011, China
[c] Department of Radiology, Minhang Hospital of Fudan University, Minhang Central Hospital, No. 170 Xinsong Road, Shanghai 201100, China
[d] Southwest JiaoTong University College of Medicine, No. 111 North 1st Section of Second Ring Road, Chengdu, 610031, China
[e] School of Biomedical Engineering, Shanghai JiaoTong University, No. 1956 Huashan Road, Shanghai, 200030, China
[f] Department of Sports Medicine, Shanghai Jiao Tong University Affiliated Sixth People's Hospital, No. 600, Yishan Road, Shanghai 200233, China
[g] Spine Institute, Shanghai University of Traditional Chinese Medicine, No.1200 Cailun Road, Shanghai 200032, China
[h] College of Chemistry, Chemical Engineering and Biotechnology, Donghua University, No. 2999, North Renmin Road, Shanghai 201620, China
[i] Department of Orthopaedics, Xinhua Hospital affiliated to Shanghai Jiaotong University School of Medicine, No.1665 Kongjiang Road, Shanghai, 200092, China

A R T I C L E   I N F O

A B S T R A C T

Critical-sized bone defect repair in patients with diabetes mellitus remains a challenge in clinical treatment because of dysfunction of macrophage polarization and the inflammatory microenvironment in the bone defect region. Three-dimensional (3D) bioprinted scaffolds loaded with live cells and bioactive factors can improve cell viability and the inflammatory microenvironment and further accelerating bone repair. Here, we used modified bioinks comprising gelatin, gelatin methacryloyl (GelMA), and 4-arm poly (ethylene glycol) acrylate (PEG) to fabricate 3D bioprinted scaffolds containing BMSCs, RAW264.7 macrophages, and BMP-4-loaded mesoporous silica nanoparticles (MSNs). Addition of MSNs effectively improved the mechanical strength of GelMA/gelatin/PEG scaffolds. Moreover, MSNs sustainably released BMP-4 for long-term effectiveness. In 3D bioprinted scaffolds, BMP-4 promoted the polarization of RAW264.7 to M2 macrophages, which secrete anti-inflammatory factors and thereby reduce the levels of pro-inflammatory factors. BMP-4 released from MSNs and BMP-2 secreted from M2 macrophages collectively stimulated the osteogenic differentiation of BMSCs in the 3D bioprinted scaffolds. Furthermore, in calvarial critical-size defect models of diabetic rats, 3D bioprinted scaffolds loaded with MSNs/BMP-4 induced M2 macrophage polarization and improved the inflammatory microenvironment. And 3D bioprinted scaffolds with MSNs/BMP-4, BMSCs, and RAW264.7 cells significantly accelerated bone repair. In conclusion, our results indicated that implanting 3D bioprinted scaffolds containing MSNs/BMP-4, BMSCs, and RAW264.7 cells in bone defects may be an effective method for improving diabetic bone repair, owing to the direct effects of BMP-4 on promoting osteogenesis of BMSCs and regulating M2 type macrophage polarization to improve the inflammatory microenvironment and secrete BMP-2.

1. Introduction

Diabetes mellitus (DM) is a chronic metabolic disease that affected 387 million individuals worldwide in 2013, and the number of patients with DM is expected to increase to over 590 million by 2035 [1]. DM increases the risk of fracture from 20% to 300% [2]. The process of bone regeneration under high-glucose conditions is markedly impaired; thus, the incidences of fracture nonunion and delayed union and the rate of compromised bone repair are high, resulting in an increased incidence of bone defects in individuals with DM [3,4]. Therefore, there is an urgent need to develop effective methods to accelerate bone repair or regeneration in patients with DM exhibiting bone defects.

Three-dimensional (3D) printing technology has been developed to fabricate scaffolds with ideal geometries and structures exhibiting precise control of pore size, porosity, and pore morphology in order to treat large-scale bone defects [5–7]. However, for patients with DM, the local microenvironment at the region of the bone defect becomes inflamed, which can lead to vascular occlusion and reduced neovascularization, and because traditional 3D-printed scaffolds usually induce cell homing, local tissue responses, and functional stimulation, these scaffolds may use the host as a bioreactor to recruit host endogenous cells for tissue regeneration; therefore, the growth and viability of loaded cells is decreased in traditional 3D-printed scaffolds [5,6,8,9]. In addition, before in vivo transplantation, 3D-printed scaffolds require cell seeding and long-term cultivation in vitro, which increases the risk of infection and lengthens the time needed for surgery [10,11]. Recently, 3D bioprinting technology was developed to facilitate rapid bone defect repair. This approach uses extrusion or jetting methods to deliver living cells in hydrogels, macromolecules, and biomaterials to generate bone tissue [9,12]. Compared with conventional 3D printing, 3D bioprinting with high numbers of loaded osteogenesis-related cells and better controllability of cell distribution and cell deposition could avoid the above limitations of 3D printing and effectively improve the osteoconductive and osteogenic potential of scaffolds, which may be helpful for accelerating bone defect repair for patients with DM [9,12–14].

Many bioinks, such as gelatin, gelatin methacryloyl (GelMA), and sodium alginate, have been used for cell loading and bone regeneration in 3D bioprinting [8]. However, it is still difficult to fabricate large-scale scaffolds with adequate printability, biocompatibility, and mechanical stability using these bioinks [15,16]. GelMA shows good printability and biocompatibility and can form covalently crosslinked hydrogels under UV light exposure [17,18]. Previous studies have shown that high-concentration GelMA possesses good shear-thinning behavior and high mechanical strength [16]. However, this material can cause some problems; for example, a high concentration of GelMA results in smaller pore sizes and lower swelling ratios, thereby reducing the diffusion of nutrients and oxygen required for the cells to survive [19]. Although low-concentration GelMA hydrogels (≤ 5 w/v%) are more suitable for cell-laden bioink owing to the high cell stability and viability [20,21], poor printability during extrusion-based 3D printing is unavoidable, as well as the poor mechanical strength and long crosslinking time [16]. To overcome these problems, some studies have focused on blending low-concentration GelMA with other components, such as gelatin, alginate, and nanoclay [16,22,23]. Previous studies have reported that low concentrations of GelMA (≤ 5 w/v%) and gelatin composite bioinks can improve the viscosity of single GelMA and provide a reversible thermo-crosslinking mechanism for gelatin upon irreversible photo-crosslinking of GelMA, thereby improving early mechanical support. Importantly, the GelMA and gelatin composite bioinks can be successfully printed and show satisfactory printability and biocompatibility [16]. In addition, gelatin gradually dissolves when the temperature increases, resulting in increased porosity and promoting the exchange of nutrients and oxygen. However, the elasticity modulus of GelMA and gelatin composite hydrogels is approximately 3–5 kPa, which can be further improved to meet the requirement of

specific tissues [16,24]. Four-arm poly (ethylene glycol) acrylate (PEG), one of the most widely utilized biomaterials for preparation of synthetic bioinks, improves the mechanical strength of hydrogels [25]. Previous studies have shown that 5–7.5% GelMA and 2.5–5% PEG bioinks can be successfully printed and possess satisfactory biocompatibility. Moreover, these hydrogels can provide up to 50–100 kPa compressive stress, which is significantly higher than that of GelMA/gelatin composited hydrogels [25]. Moreover, PEG has high water content and exhibits nonfouling and viscoelastic properties, making it highly biocompatible and tunable within hydrogels and allowing for the expansion and growth of laden cells [26,27]. However, few studies have evaluated the biochemical characteristics of GelMA/gelatin/PEG hybrid hydrogels.

In addition to bioinks, appropriate loading of cytokines is another important factor affecting 3D bioprinting for bone defect repair. DM is an inflammatory disease characterized by elevated levels of pro-inflammatory cytokines, such as interleukin (IL)-1β, IL-6, and C-reactive protein [28]. However, current approaches developed for bone regeneration in DM directly target osteoblasts or osteoclasts, and other critical roles of inflammation control under diabetic conditions have not been thoroughly studied, leading to limited improvement of the healing process [29–32]. Macrophage polarization plays key roles in the regulation of inflammation, and the ratio of M2/M1 type macrophages is significantly reduced in patients with DM, resulting in inflammatory damage to the body that cannot be repaired through self-regulation [33]. In particular, in the bone defect region in patients with DM, classical activated macrophages (M1 type macrophages) dominate in the pro-inflammatory state, and many pro-inflammatory cytokines (such as IL-1β, IL-6 and tumor necrosis factor [TNF]-α) secreted by M1 type macrophages inhibit the osteogenic differentiation of bone marrow mesenchymal stem cells (BMSCs) and osteoblasts by affecting multiple signaling pathways, further promoting their apoptosis and the differentiation of monocytes to osteoclasts [31,32,34–36]. At the same time, selectively activated macrophages (M2 type macrophages), which inhibit the inflammatory response, are gradually consumed in the inflammatory body of DM, disrupting self-regulation of the body's inflammatory damage status and inhibiting macrophage polarization to the M2 type. Thus, the roles of M2 type macrophages in secreting anti-inflammatory cytokines (e.g., IL-4, IL-10, IL-1Rα, arginase-1) and promoting the repair of damaged tissues and neovascularization are eliminated [37]. Additionally, the secretion of transforming growth factor-β (TGF-β), osteopontin (OPN), and bone morphogenic protein-2 (BMP-2) by M2 type macrophages is also reduced, further inhibiting the migration and osteogenic differentiation of BMSCs and eventually leading to bone repair failure [31,32].

Therefore, in 3D-bioprinted scaffolds, appropriate loading of bioactive factors that could promote osteogenesis and M2 type macrophage polarization is critical for bone defect repair in patients with DM. BMP-4, which belongs to the TGF-β superfamily, can directly induce osteogenic differentiation of BMSCs and osteoblasts through the Smad signaling pathway [38]. Recently, many studies have reported that the expression of BMP-4 is decreased in the serum of patients with DM and the calvarial defects of a DM rat model [39,40]. In addition, Martínez et al. and Valencia et al. reported that BMP-4 could induce macrophages to the M2 type by enhancing the secretion of IL-10 [41,42]. Therefore, BMP-4 may be a viable loading cytokine for 3D bioprinting to stimulate the healing of bone defects in patients with DM.

A scaffold-based controlled sustained release system for local dissemination of BMP-4 can prolong the release period and extend the functional half-life of this factor [43]. Mesoporous silica nanoparticles (MSNs) have attracted much attention in the small molecule delivery field owing to their desirable characteristics [44–46]. For example, MSNs possess an open-pore structure, and the sizes of the pores and the MSNs themselves can be controlled synthetically [44,45]. Previous studies have reported that macroporous MSNs can load BMPs through physical encapsulation and realize continuous release [44,45]. Additionally, the printability of hydrogels for 3D printing was not

obviously affected after addition of MSNs [44,45]. However, the effects of MSNs on the characteristics of bioinks and 3D bioprinted scaffolds have not been elucidated.

In this study, we aimed to evaluate the incorporation of MSNs in GelMA/gelatin/PEG bioinks to construct composite bioinks for 3D bioprinting. Additionally, we examined the biofunctions of BMP-4 and its sustainable release from MSNs for modulation of macrophage polarization and inhibition of inflammation in order to assess the roles of BMP-4 and M2 type macrophages in osteogenic differentiation of BMSCs and in a calvarial defect repair model in DM rats.

2. Methods

2.1. Synthesis of large macroporous MSNs

Large macroporous MSNs were prepared as previously described [46]. Briefly, 1 g cetrimonium bromide was dissolved in an emulsion made of 150 mL deionized water, 20 mL ethanol, 40 mL ethyl ether, 2 mL aqueous ammonia, and 0.1125 g calcium nitrate (Ca$(NO_3)_2$.4H$_2$O). After vigorously stirring at 25 °C for 30 min, 600 μL tetraethyl orthosilicate was added to the mixture. The molar ratio of Si:Ca was 85:15. The mixture was vigorously stirred at 30 °C (a temperature shown to increase pore size) for 4 h. A white precipitate was obtained, filtered, washed with pure water, dried in air at 60 °C for 24 h, and calcined at 550 °C for 5 h to prepare MSNs.

2.2. Preparation of bioinks for material tests

The compositions of different bioinks (Table 1) were used to evaluate the characteristics of the materials. All procedures were performed in the dark. Briefly, freeze-dried GelMA polymers (EFL-GM-90; Suzhou Intelligent Manufacturing Research Institute, Suzhou, China) were dissolved in deionized water in glass bottles with rotator at 40 °C and maintained for 1 h to form homogeneous solutions. Next, gelatin (VETEC, USA), PEG (JenKem Technology, Beijing, China), lithium phenyl-2,4,6-trimethylbenzoylphosphinate (LAP, SE-3DP; StemEasy, Jiangyin, China), and MSNs were successively added into the GelMA solutions, and the solutions were continuously stirred at 40 °C for 1 h in a water bath. Finally, homogeneous bioinks was successfully obtained.

2.3. Material characterization

2.3.1. Printability

5%GelMA/2%gelatin/2%PEG, 5%GelMA/3%gelatin/2%PEG, and 5%GelMA/5%gelatin/2%PEG were prepared to preliminarily investigate the printability. In brief, above bioinks were printed using a 2-mL syringe equipped with a 0.26 mm inner diameter needle [16].

2.3.2. Rheology

The rheological characteristics of the prepared bioinks were evaluated using a rheometer (HAAKE MARS 60; Germany). A 50-mm-diameter plate-plate geometry was used in all tests. First, all samples were placed on the plate at 40 °C to completely fill the 1-mm gap between the two plates. Tests of viscosity and shear stress were performed by varying the shear rate from 1 to 500 s^{-1} with rotational tests at 20 °C. The viscosity was then measured with the temperature ramped from 37

to 15 °C at a rate of 1 °C min^{-1}. The shear rate was maintained at 1 s^{-1}. The storage modulus (G′) and loss modulus (G″) were tested as a function of temperature at a constant frequency of 1 Hz and a constant strain of 0.1%, whereas the hydrogel samples were equilibrated at 40 °C and then cooled at a rate of 1 °C min^{-1} from 40 to 10 °C.

2.3.3. Mechanical properties

The compressive strength of the prepared bioinks was measured with a testing machine (HY–940FS; Hengyu, China) with a speed of 1 mm min^{-1}. For unconfined tests, the composite bioinks were cured in the disks (5 mm thick and 10 mm diameter) by being exposed to 365 nm ultraviolet (UV) light (1 W cm^{-2}) for 2 min. Five parallel samples were used in the experiments.

2.3.4. Swelling test

To measure the swelling of composite hydrogels, the 5%GelMA/3%gelatin/2%PEG/0.4%MSNs (denoted as GelMA/gelatin/PEG/0.4% MSNs) bioinks were cured in the standard mold (length × width × height: 8 mm × 8 mm × 2 mm) by being exposed to 365 nm UV light (1 W cm^{-2}) for 2 min. Three parallel samples were lyophilized and weighed to determine the dry weight of each sample (W$_0$). Then, above samples were immersed into PBS at 37 °C. After immersing for different time points, the samples were rubbed with a filter paper to remove the excess water, and the swollen weight of each samples was recorded (W$_x$). The swelling ratio was then calculated as Q $= (W_x – W_0)/W_0*100$ [47].

2.3.5. Degradation test in vitro and in vivo

Above methods in swelling test were used to fabricate standard samples to measure the degradation of the GelMA/gelatin/PEG/0.4% MSNs composite hydrogels. The samples were incubated with collagenase II (2U/ml, BioFroxx, Germany) at 37 °C. The collagenase solution was refreshed weekly. After immersing 1, 3, 5, 7, 14, and 21 days, samples were removed. The samples were subsequently lyophilized and weighed to determine the dry weight of each sample (W$_t$), and the dry weight of 0 day was recorded as W$_{dry}$. The degradation ratio was then calculated as DR $= (W_{dry} – W_t)/W_{dry}*100\%$ [47]. Then, above sterile samples were fabricated, and implanted subcutaneously on the back of C57BL/6 mouse. After implanting 7, 14, and 21 days, mice were routinely executed, and the samples were carefully cleaned to remove the adjacent tissue. The same methods were used to calculate degradation ratio [47,48]. Three parallel samples were used in the experiments.

2.3.6. Material composition and morphology

The morphologies of MSNs were evaluated by transmission electron microscopy (TEM, JEM-2100F; JEOL, Japan), and the average diameter of MSNs was calculated from the TEM images of five independent regions. Nitrogen adsorption–desorption measurement was conducted with a ASAP 2420 (Micromeritics, USA) surface area and pore size analyzer. Pore size and surface area of MSNs were analyzed by the Barrett–Joyner–Halenda (BJH) and Brunauer–Emmett–Teller (BET) methods, respectively. Then the surface morphology of composite hydrogels with or without MSNs were observed by scanning electron microscopy (SEM, TM-1000; Hitachi, Japan). The pH value of GelMA/gelatin/PEG/0.4% MSNs solution was evaluated by pH meter (FiveEasy; Mettler Toledo, Switzerland).

2.4. Loading of MSNs with BMP-4 and evaluation of BMP-4 release

For loading of BMP-4, 1 μg mL^{-1} BMP-4 (R&D Systems, Minneapolis, MN, USA) was added to 1 mg mL^{-1} MSNs dissolved in phosphate-buffered saline (PBS). Vortex oscillation was then carried out for 10 s. The solution was shaken at room temperature (25 °C) for 24 h in the dark. After centrifugation at 8000 rpm for 8 min, the supernatant was used to assess the loading content, and the remaining sediment was

Table 1
The compositions of different bioinks.

Bioinks	GelMA	Gelatin	LAP	PEG	MSNs
GelMA/gelatin/PEG	5%	3%	0.2%	2%	–
GelMA/gelatin/PEG/0.4% MSNs	5%	3%	0.2%	2%	0.4%
GelMA/gelatin/PEG/0.8% MSNs	5%	3%	0.2%	2%	0.8%

Units = w/v %.

the MSNs/BMP-4.

The release of BMP-4 from MSNs was then assessed. The MSNs/BMP-4 mixture was added to 1.5-mL EP tubes with 1 mL simulated body fluid (SBF; Leagene Biotechnology, Beijing, China) at room temperature with shaking at 120 rpm. After 12 h or 1, 3, 5, 7, 9, 14, 21, or 28 days, the EP tubes were centrifuged at 2000 rpm for 3 min, and all supernatants were collected and supplemented with SBF. A BMP-4 enzyme-linked immunosorbent assay kit (Abcam, USA) was used to evaluate the concentrations of the supernatants according to the manufacturer's instructions. Five parallel samples were used in the experiments.

2.5. Isolation and culture of primary BMSCs

Five healthy 3-week-old male Sprague-Dawley rats were purchased from the Animal Laboratory of Shanghai Jie-Si-Jie Co. (Shanghai, China). As previously described, all rats were euthanized and immersed in 75% alcohol for 5 min. Then, soft tissue was dissected from both lower limbs using sterile operation methods. The whole marrow was flushed out of the bone cavities thoroughly by drawing and expelling with a 1-mL syringe using PBS five times. Marrow aspirates were filtered using a 70-μm nylon mesh filter and centrifuged. Next, BMSCs were cultured with α-MEM medium (Hyclone, Logan, UT, USA) supplemented with 10% fetal bovine serum (FBS; Gibco, Paisley, UK), 1% penicillin-streptomycin (Hyclone), and 0.4% gentamicin (Sangon Biotech, Shanghai, China), and the medium was replaced every 3–4 days. The cells were used at passages 3–5.

2.6. RAW264.7 cell culture

RAW264.7 cells were obtained from the Cell Bank of the Chinese Academy of Sciences (Shanghai, China) and cultured with high-glucose Dulbecco's modified Eagle's medium (DMEM; glucose concentration: 25 mM; Hyclone) supplemented with 10% FBS (Gibco), 1% penicillin-streptomycin, and 0.4% gentamicin.

2.7. Bioink preparation and the 3D bioprinting process

According to the experimental grouping, MSNs/BMP-4 (BMP-4:MSNs = 1 μg:1 mg), BMSCs, and RAW264.7 cells were added to 5% GelMA, 3% gelatin, 2% PEG, and 0.2% LAP composite bioinks (Table 2). Finally, homogeneous bioinks were successfully obtained.

Scaffolds were fabricated using 3D-Bioplotter (Bio-Architect; Regenovo, Hangzhou, China). Bioink solutions were sterilized using a 0.22-μm filter unit (Millipore, Billerica, MA, USA). Next, bioinks were loaded into plastic sterile syringes barrel and subjected to rapid thermo-crosslinking by adjusting the syringe barrel temperature controller between 12 and 22 °C for stable filament deposition. The temperature of the bottle platform was adjusted to 1–4 °C lower than the syringe temperature to maintain the printed scaffolds. Then, printed scaffolds were placed under a temporary UV light source (365 nm, 0.5 W cm^{-2}) for fast curing. After the whole printing process, the scaffolds were

exposed to UV light for 2 min for long-term stability by photo-crosslinking of GelMA. All 3D bioprinting processes were performed at room temperature in the dark, with sterile procedures.

2.8. Cell viability assay

After incubation in conditioned medium, Live-Dead staining was performed on day 1, and Cell Counting Kit-8 (CCK-8) assays were performed on day 1, 3, 5, and 7 to assess cell viability. Briefly, after washing twice with PBS to remove excess medium from the scaffolds, three scaffolds were visualized with fluorescent dyes (Live Dead Cell Kit; KeyGEN, Biotech, Nanjing, China) at 37 °C for 30 min. Then, scaffolds were rinsed twice with PBS and analyzed using fluorescence microscopy. Image Pro Plus 6.0 software (NIH) was used to evaluate cell viability in the fluorescence images (cell viability [%] = number of live cells/number of total cells × 100). In addition, the other three scaffolds were rinsed with PBS and incubated in 10% CCK-8 reagent (Dojindo, Kumamoto, Japan) containing medium for 2 h at 37 °C, and the absorbance was then determined at 450 nm using a spectrophotometer (Infinite M200 Pro; Tecan, Switzerland).

2.9. Assessment of macrophage polarization

The polarization of RAW264.7 cells in the RAW and RAW/BMP-4 groups was assessed by fluorescence staining to evaluate the expression levels of CCR7 (red, M1 marker) and CD206 (green, M2 marker). Briefly, after incubation in high-glucose DMEM for 2 and 5 days, scaffolds were fixed with 4% paraformaldehyde (Biosharp, Hefei, China) for 15 min, permeabilized with 0.1% Triton-X for 30 min, and blocked using 5% bovine serum albumin (BSA) for 1 h. Samples were incubated with M1 primary polyclonal IgG rabbit anti-mouse antibodies for CCR7 (1:100; Abcam) overnight at 4 °C and then with secondary goat anti-rabbit Alexa Fluor 594 antibodies (1:500; Abcam) for 2 h at room temperature. Next, samples were incubated with M2 primary polyclonal IgG mouse anti-mouse antibodies for CD206 (1:50; Abcam) overnight at 4 °C and then with secondary goat anti-mouse Alexa Fluor 488 antibodies (1:500; Abcam) for 2 h at room temperature. Finally, the nuclei were stained blue with 4′,6-diamidino-2-phenylindole, dihydrochloride (DAPI) for 5 min and observed with a fluorescence confocal microscope (Leica, Germany). Image Pro Plus 6.0 software (NIH) was used to quantitatively analyze the fluorescence intensities of CCR7 and CD206 for five different view regions from three independent scaffolds.

2.10. Gene expression levels of inflammatory factors

The gene expression levels of pro-inflammatory factors. including IL-1β, IL-6, and TNF-α, and anti-inflammatory factors, including IL-1Rα, IL-4, and IL-10, were assessed by quantitative real-time polymerase chain reaction (qRT-PCR). Briefly, different scaffolds were incubated in high-glucose DMEM for 2 days, and total RNA was extracted using a Qiagen RNeasy Mini kit (Valencia, CA, USA) and subjected to cDNA synthesis. qRT-PCR was performed using a SYBR Premix Ex TaqTM kit (TaKaRa, Otsu, Japan) and an Applied Biosystems 7500 Real-Time PCR System (Applied Biosystems, Foster City, CA, USA). qRT-PCR was performed in triplicate using the following cycling parameters: initial denaturation at 95 °C for 30 s; 40 cycles of denaturation at 95 °C for 5 s and annealing at 60 °C for 34 s. The sequences of primers are listed in Supplemental Table 2, and glyceraldehyde-3-phosphate dehydrogenase was used as a quantitative control for RNA levels.

2.11. BMP-2 expression evaluation

The expression levels of BMP-2 in RAW264.7 cells in the RAW and RAW/BMP-4 groups were assessed by fluorescence staining. Briefly, after incubation in high-glucose DMEM for 3 days, scaffolds were fixed

Table 2
Compositions of cell-loaded bioinks for 3D bioprinting.

Groups	Bioink composition (w/v)	MSNs/BMP-4 (w/v)	RAW264.7 amount (mL^{-1})	BMSCs amount (mL^{-1})
RAW	5% GelMA, 3% Gelatin, 2% PEG, 0.2% LAP	–	10^7	–
BMSC		–	–	10^7
RAW/BMP-4		0.4%	10^7	–
BMSC/BMP-4		0.4%	–	10^7
BMSC/RAW		–	10^6	10^7
BMSC/RAW/BMP-4		0.4%	10^6	10^7

with 4% paraformaldehyde (Biosharp) for 15 min, permeabilized by 0.1% Triton-X for 30 min, and blocked using 5% BSA for 1 h. Samples were then incubated with primary polyclonal IgG rabbit anti-mouse antibodies targeting BMP-2 (1:100; Abcam) overnight at 4 °C and then with secondary goat anti-rabbit Alexa Fluor 594 antibodies (1:500; Abcam) for 2 h at room temperature. The cytoskeleton was stained with phalloidin (ThermoFisher, USA) for 2 h at room temperature, and the nuclei were stained blue with DAPI (ThermoFisher) for 5 min. A fluorescence confocal microscope (Leica) was used to acquire representative images. Image Pro Plus 6.0 software (NIH) was used to quantitatively analyze the fluorescence intensity of BMP-2 in five different views for three independently prepared scaffolds.

2.12. Osteogenic differentiation of BMSCs in 3D-bioprinted scaffolds

Representative proteins (Runx2 and OPN) indicating osteogenic differentiation were evaluated in the BMSC, BMSC/BMP-4, BMSC/RAW, and BMSC/RAW/BMP-4 groups by fluorescence staining. Briefly, after culture of cells in conditioned medium for 12 days, scaffolds were fixed with 4% paraformaldehyde (Biosharp) for 15 min, permeabilized with 0.1% Triton-X for 30 min, and blocked with 5% BSA for 1 h. Samples were then incubated with primary polyclonal IgG rabbit anti-rat antibodies targeting Runx2 (1:500; Abcam) and OPN (1:200; Abcam) overnight at 4 °C and then with secondary goat anti-rabbit Alexa Fluor 594 antibodies (1:200; Abcam) for detection of Runx2 or secondary goat anti-rabbit Alexa Fluor 488 antibodies (1:500; Abcam) for detection of OPN for 2 h at room temperature. The cytoskeleton was stained with Alexa Fluor 488 for detection of Runx2 or Alexa Fluor 594 phalloidin (ThermoFisher) for detection of OPN for 2 h at room temperature. Nuclei were stained with DAPI for 5 min. A fluorescence confocal microscope (Leica, Germany) was used to acquire representative images. Image Pro Plus 6.0 software (NIH) was used to quantitatively analyze the fluorescence intensity of Runx2 and OPN in five different views for three independent scaffolds.

2.13. Alkaline phosphatase (ALP) and Alizarin red staining

After incubation on conditioned medium for 5 days, scaffolds for the BMSC, BMSC/BMP-4, BMSC/RAW, and BMSC/RAW/BMP-4 groups were fixed with 4% paraformaldehyde for 15 min and blocked with 1% BSA for 1 h. ALP staining was then performed for detection of ALP activity using an ALP kit (Beyotime, Shanghai, China) according to the manufacturer's instructions. After incubation on the scaffolds for 21 days, the scaffolds were fixed and stained with Alizarin red dye (Cyagen, Guangzhou, China) according to the manufacturer's instructions. Image Pro Plus 6.0 software (NIH) was used to quantitatively analyze the staining intensity of ALP and Alizarin red for five different independently prepared scaffolds.

2.14. Animal study

2.14.1. Calvarial defect model in DM rats

Four-week-old male Sprague-Dawley rats were fed with a high-fat diet for 4 weeks and administered a single low dose (30 mg kg^{-1}) of streptozotocin (STZ) via intraperitoneal injection to establish the type 2 DM model. After 7 days of STZ injection, blood was collected by tail cutting to test random plasma glucose levels (PGLs) using a glucometer. Rats with a PGL above 16.7 mM were considered diabetic, and rats with a PGL below this value were excluded [49]. Thirty-six rats from the DM model were used to establish a calvarial defect model [50], and the average PGLs of above DM rats was 20.76 ± 1.56 mM. Briefly, all rats were anesthetized with an intraperitoneal injection of 1% pentobarbital (10 μL g^{-1}). After sterilization with povidone iodine, the skin was prepared, and sterile dressing was applied to the calvarial area. Then, a 5 mm diameter calvarial defect was made using a circular bit on both sides, being careful to avoid damaging the brain tissue. Different

scaffolds after 3D bioprinting were placed in the right defect area, and the left side holes were as the control. Finally, the skin was sutured, and the wound was disinfected. The use of rats and all related procedures in this study were approved by the Shanghai Ninth People's Hospital, Shanghai Jiao Tong University School of Medicine Animal Care and Use Committee and complied with the guidelines of the National Institutes of Health Guide for Care and Use of Laboratory Animals (approval no. GB14925-2010).

2.14.2. Immunohistochemistry and imaging analysis

Three days after surgery, six random rats from the RAW and RAW/BMP-4 groups were sacrificed. Paraffin-embedded sections of the calvarial defect area were routinely prepared and subjected to immunohistochemical staining. Briefly, tissue sections (5 μm thick) were deparaffinized, rehydrated in a series of descending concentrations of ethanol, and placed in an antigen retrieval solution (20 min microwave irradiation in 0.1 M PBS, pH 7.4). Then, endogenous peroxidase was blocked using 3% H_2O_2. After three rinses in PBS for 5 min each, nonspecific binding was blocked by incubation in 10% normal rabbit serum for 30 min at room temperature. Then, the sections were incubated with primary polyclonal anti-M1 antibodies (1:5000; Servicebio, Wuhan, China) and primary polyclonal anti-M2 antibodies (1:200; Servicebio), followed by incubation with secondary goat anti-rabbit Alexa Fluor 594 antibodies (1:200; Abcam) for M1 or Alexa Fluor 488 antibodies for M2 (1:500; Abcam). Nuclei were stained with DAPI for 10 min. Then, additional sections from the above specimens were incubated with primary polyclonal anti-IL-1β antibodies (1:600; Servicebio) and primary polyclonal anti-IL-10 antibodies (1:200; Servicebio), followed by incubation with secondary goat anti-rabbit horseradish peroxidase-conjugated antibodies (1:200; Servicebio). Immunoreactivity was visualized using a DAB chromogenic reagent (DAKO, Glostrup, Denmark). Sections were counterstained with hematoxylin for 3 min. A fluorescence microscope (Eclipse C1, Nikon, Japan) was used to acquire representative images. Image Pro Plus 6.0 software (NIH) was used to quantitatively analyze the fluorescence intensities of CCR7, CD206, IL-1β, and IL-10 in five different views from all specimens.

2.14.3. Micro-computed tomography (micro-CT)

Two months after surgery, 24 rats from the BMSC, BMSC/BMP-4, BMSC/RAW, and BMSC/BMP-4/RAW groups were sacrificed, and skulls were removed intact. All samples were examined on a micro-CT scanning system (Bruker skyscan1176; Germany). Briefly, the specimens were scanned with a spot size of 10 μm, current of 250 μA, and maximum voltage of 40 kV. After scanning, 3D images were reconstructed. The bone volume fraction (BV/TV), and bone mineral density (BMD) were calculated using auxiliary software.

2.14.4. Hematoxylin and eosin (HE) and masson staining

After micro-CT examination, calvarial specimens with different scaffolds were fixed with 4% paraformaldehyde, decalcified in 10% ethylenediaminetetraacetic acid, embedded in paraffin, and sectioned at a thickness of 5 μm. The sections were stained with HE and Masson staining and observed by light microscopy (Leica, Germany).

2.15. Statistical analysis

Statistical analysis was performed with SPSS version 19.0 (IBM, Armonk, IL, USA). All results are shown as means ± standard deviations. Results were analyzed by independent t-tests and one-way analysis of variance. Results with P values of less than 0.05 were considered significant.

3. Results and discussion

3.1. Bioink formulation and characterization

It is essential to select the appropriate bioink for extrusion-based 3D bioprinting to meet many necessary requirements of printability, mechanical strength, and biocompatibility, and effective bioprinted scaffolds could provide a suitable environment for effective cell growth, differentiation, and tissue formation. In this study, the composite bioink designed contained certain percentages of GelMA, gelatin, PEG, and MSNs to facilitate 3D bioprinting. The crosslinking and inner modification mechanism of the GelMA/gelatin/PEG hydrogel were showed in Fig. S1, and gelatin was reversible thermo-crosslinking, and GelMA and PEG was irreversible photo-crosslinking during 3D bioprinting.

As shown in Fig. S2 and Supplement Table 1, the TEM image of MSNs showed the large mesoporous structure with an average particle size of 139.7 nm. The surface area and pore size of as-prepared MSNs were 541.6 m^2/g and 8.9 nm, respectively, which was similar with previous study [46]. Therefore, the MSNs with large pores was successfully prepared and could be used for BMP-4 loading in this study.

The results of printability test showed that the extruded filaments at the nozzle outlet were irregular and not smooth for 5%GelMA/2%gelatin/2%PEG, while 5%GelMA/3%gelatin/2%PEG and 5%GelMA/5% gelatin/2%PEG could form uniform and smooth filaments (Fig. S3). Thus, the 5%GelMA/3%gelatin/2%PEG was considered as printable bioinks and employed in the following studies.

Furthermore, we evaluated the rheological characteristics of the

materials to further determine printability. As shown in Fig. 1A, adding MSNs enhanced the shear-thinning behavior of GelMA/gelatin/PEG bioinks, and the high viscosity after printing enabled the scaffold to maintain its structures with high resolution (Fig. 1G–I). As shown in Fig. 1B, the viscosity of MSNs-based bioinks decreased dramatically when the temperature was increased from 20 °C to 25 °C. Additionally, GelMA/gelatin/PEG/0.4% MSNs bioinks remained liquid at 37 °C, but transformed into a gel state at 20 °C (Fig. S4A and S4B). Thus, the tunable viscosity of the composite bioink facilitated the formation of stable filaments by changing the temperature of the nozzle and syringe barrel as appropriate for living cells. As shown in Fig. 1C, as a thermo-reversible crosslinking hydrogel, gelatin induced rapid thermo-crosslinking of all bioinks, instantly maintaining the structure of the printed filaments and yielding a finer shape.

As shown in Fig. 1D and E, the compressive strength of GelMA/gelatin/PEG hydrogels reached up to approximately 121.26 ± 6.33 kPa. In addition, after adding MSNs, the compressive strength and elasticity modulus of GelMA/gelatin/PEG/MSNs hydrogels was significantly higher than that of GelMA/gelatin/PEG hydrogels, which enabled the scaffold shape to be maintained. Moreover, the compressive strength and elasticity modulus of 0.4% MSNs-based hydrogels were approximately 194.63 ± 9.58 and 46.41 ± 2.60 kPa, respectively; those for the 0.8% MSNs-based hydrogel were 233.06 ± 8.35 and 56.09 ± 2.52 kPa, respectively. Because 0.4% MSNs was sufficient to load necessary BMP-4 and because the rheological and mechanical results were not obviously different compared with those of the 0.8% MSNs-based bioink, we chose the 0.4% MSNs-
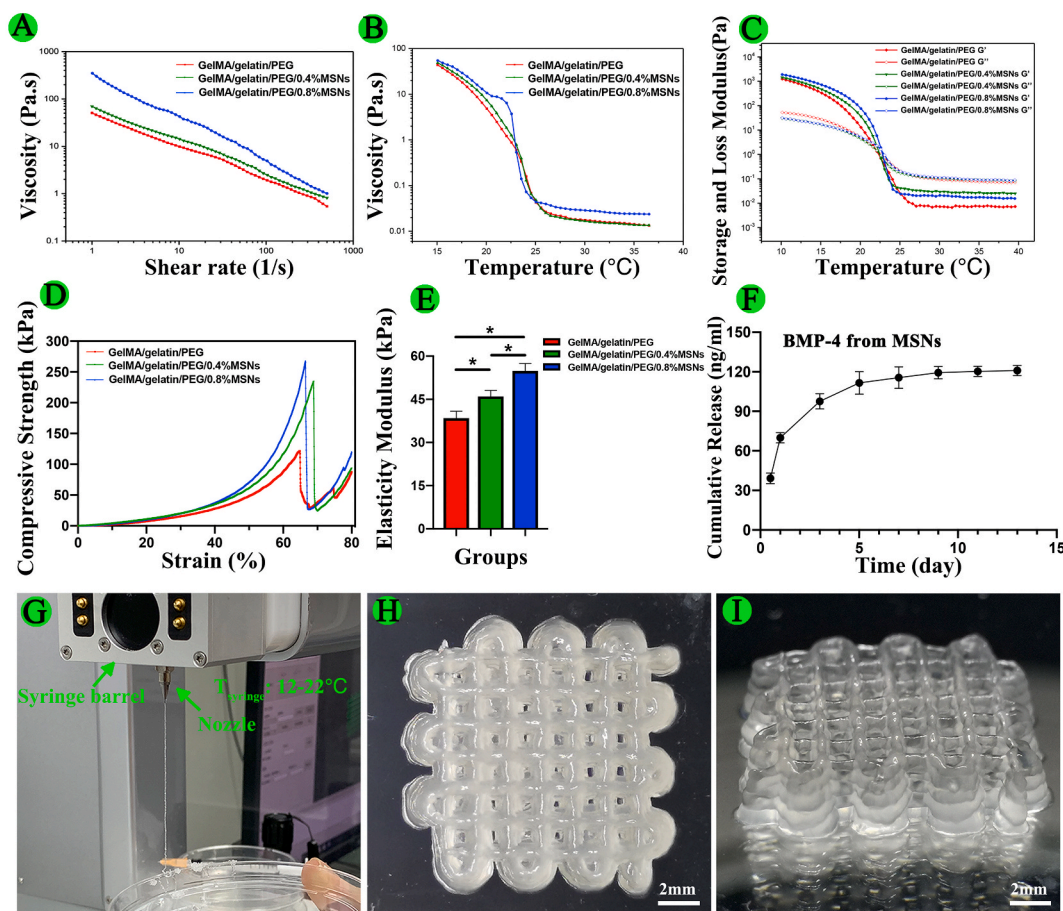
Fig. 1. Characterization of the bioink and 3D-bioprinted scaffolds. (A) Viscosity as a function of shear rate at 20 °C. (B) Viscosity as a function of temperature. (C) Effects of temperature on the storage modulus (G′) and loss modulus (G″). (D) Compressive stress-strain curves. (E) Elasticity modulus. (F) Cumulative release of BMP-4 from MSNs at different times. (G) 3D bioprinting process (T$_{syringe}$ means the temperature of the syringe barrel). (H, I) Top and side views of the 3D-bioprinted scaffold (*$P < 0.05$).
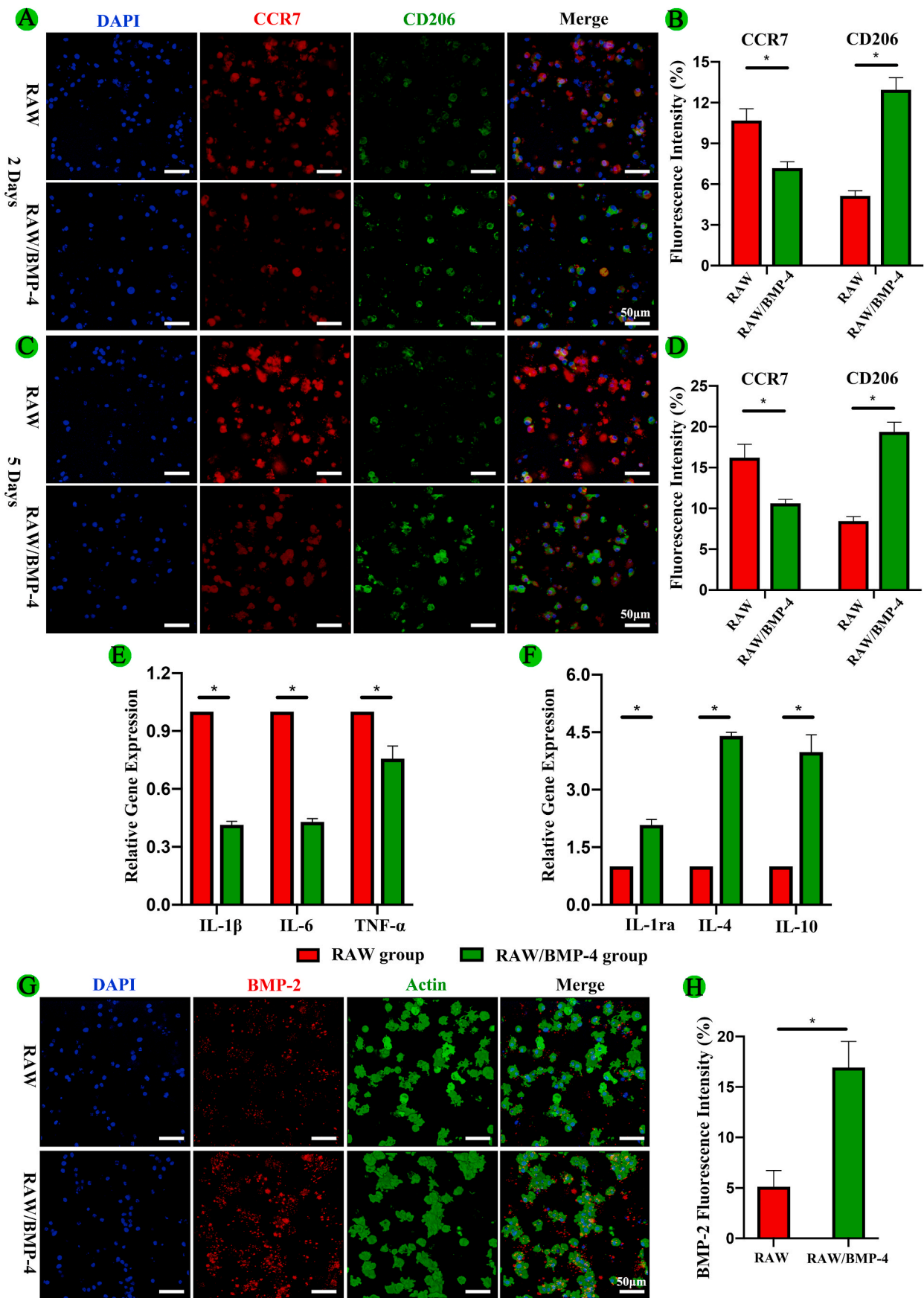
Fig. 2. Polarization and expression of inflammatory cytokines and BMP-2 in RAW264.7 macrophages in the 3D-bioprinted scaffolds. (A, B) Fluorescence staining and quantification of an M1 marker (CCR7) and M2 marker (CD206) at 2 days. (C, D) Fluorescence staining and quantification of an M1 marker and M2 marker at 5 days. (E, F) Expression of genes encoding the selected inflammatory cytokines. (G, H) Fluorescence staining and quantification analysis for BMP-2 ($*P < 0.05$).
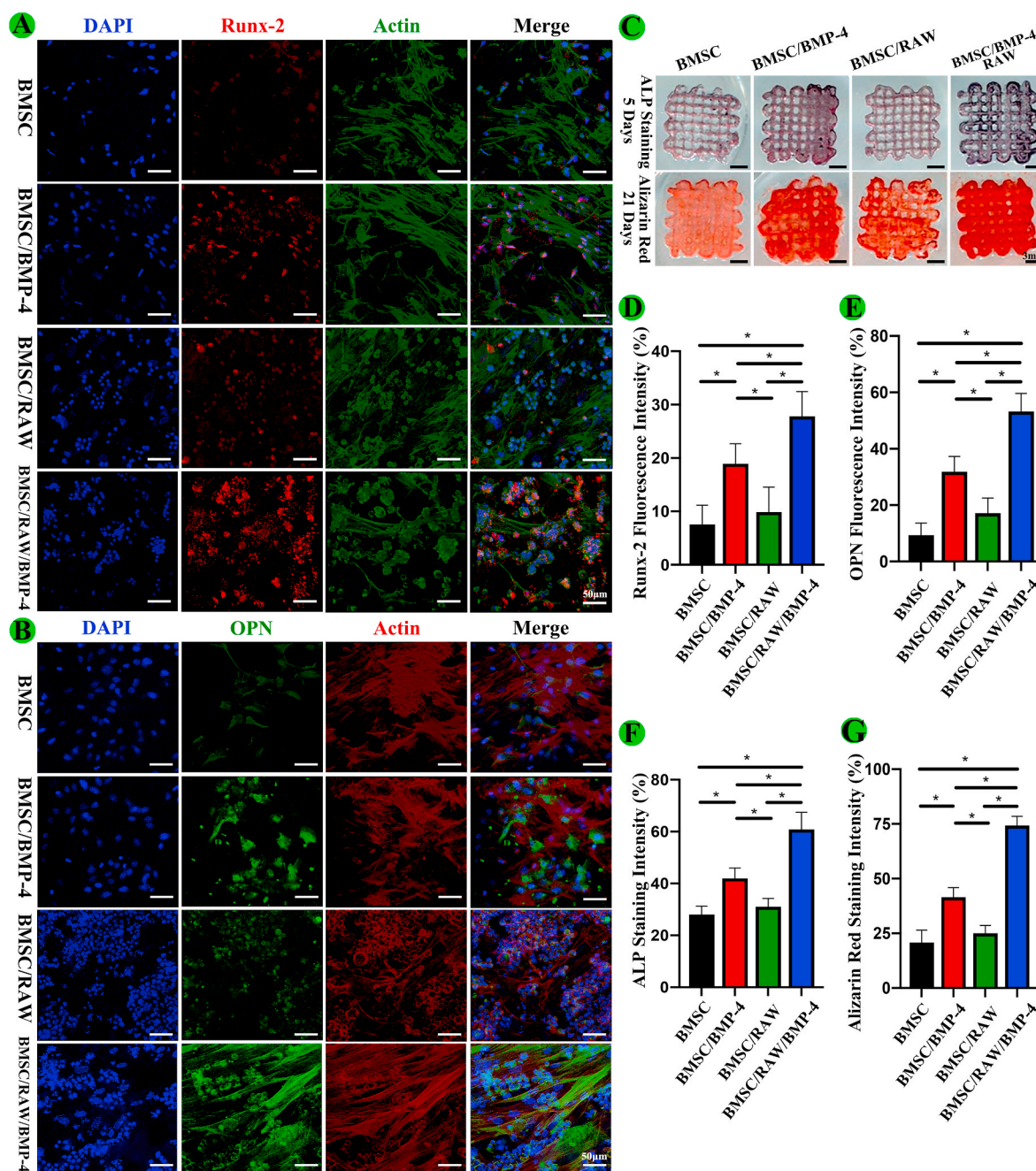
Fig. 3. Osteogenic differentiation of BMSCs in the 3D-bioprinted scaffolds. (A, B) Fluorescence staining for Runx2 and OPN. (C) ALP and Alizarin red staining. (D–G) Quantitative analyses of the above assays (*$P < 0.05$).

based bioink in order to minimize the influence of Si iron on macrophage polarization and osteogenesis [46,51,52]. This GelMA/gelatin/PEG/0.4% MSNs bioink could be successfully composited and printed (Fig. 1G–I). Additionally, the bioink showed the reversible thermo-crosslinking characteristics of gelatin, which could help to regulate the printability of the material following adjustment of the temperature of the nozzle and syringe barrel in the printer head and induce rapid thermo-crosslinking to maintain the shape of the printed filaments. Furthermore, the bioink possessed the irreversible photo-crosslinking ability of GelMA, which could help to maintain the special structure of 3D bioprinted scaffolds for a long time. This formulation also resulted in good mechanical strength. What's more, we found that MSNs could be embedded in the polymer matrix of hydrogel (Fig. S4C and S4D) due to the nano-scaled particle size. In the previous study [53], it suggested

that the porosity of the hydrogel-based scaffold could be affected by the incorporation of MSNs into the polymer matrix when the feeding ratio of MSNs up to 5%. However, the used content of MSNs in this study was only 0.4%, thus such low ratio of MSNs might have no obvious influence on the porosity of the hydrogel.

As shown in Fig. S5, the swelling ratio of GelMA/gelatin/PEG/0.4% MSNs hydrogel had continually increased within the first 5 h of immersion in PBS, and reached 582.92 ± 19.36% at 24 h immersion, which was similar with previous studies [47,54]. The good swelling ability of above hydrogel could provide a moist environment for the cells to grow, and increase the diffusion of nutrients and oxygen required for the cells to survive [19,47,54]. In addition, the degradation ratio of GelMA/gelatin/PEG/0.4%MSNs hydrogel respectively was 55.53 ± 1.99% in vitro and 47.12 ± 1.57% in vivo for 21 days.
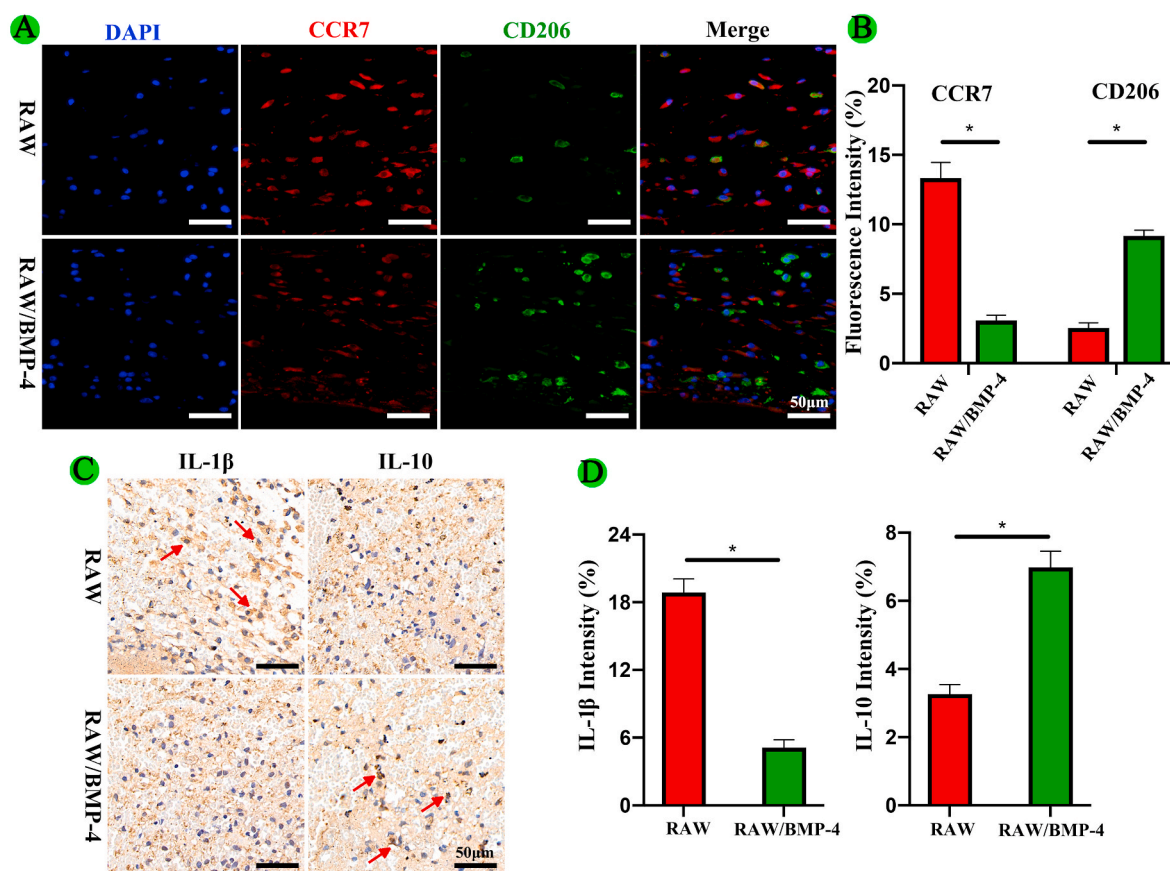
Fig. 4. Polarization of and expression of inflammatory factors in RAW264.7 macrophages for different groups in vivo. (A, B) Fluorescence staining and quantification of CCR7 and CD206. (C, D) Immunohistochemical staining and quantification of IL-1β and IL-10 (the arrow indicates the immunopositive cells; *$P < 0.05$).

Almost 53% mass of polymer matrix was residual after in vivo implantation, which was helpful for maintaining the early special three-dimensional structure of the scaffolds [47,48]. Thus, the biodegradable characteristic not only could maintain the release of BMP-4 from hydrogel, but also provide sufficient space for cell growth and tissue ingrowths when implanted into the bone defect [46,55].

3.2. Sustained release of BMP-4 from MSNs

In our study, we prepared macroporous MSNs and added them into GelMA/gelatin/PEG hydrogels. Then, we added 1 μg mL^{-1} BMP-4 to 1 mg mL^{-1} MSNs to evaluate the loading and cumulative release of BMP-4 from MSNs. The results showed that the loading rate was approximately 48.52% ± 4.67% and that BMP-4 exhibited sustained release from MSNs in vitro (Fig. 1F), consistent with previous studies [46]. Accordingly, BMP-4-loaded MSNs were mixed with GelMA, gelatin, and PEG to yield BMP-4-loaded hydrogels for subsequent experiments. According to previous studies, the release concentration of BMP-4 used in our study was sufficient to induce macrophage polarization and osteogenic differentiation of BMSCs [41,56]. In addition, the pH condition is an important factor to affect the drug release from nanocarrier. Thus, we detected the pH value of GelMA/gelatin/PEG/0.4%MSNs solution. It was found that the pH value of GelMA/gelatin/PEG/0.4%MSNs solution was measured to be 7.22 ± 0.04, which was close to the pH of SBF solution (pH = 7.4). Therefore, it was considered that the release behavior of BMP-4 from MSNs in the hydrogels might be the same.

3.3. Biocompatibility of scaffolds

To identify whether the bioink component, printing process, and UV crosslinking may affect the viability of loaded cells for different groups, we performed Live/Dead assays and CCK-8 assays. The results of Live/Dead assays showed that more than 90% of cells were viable on day 1 in all groups (Fig. S6A and S6B). Moreover, the results of CCK-8 assays showed that cells were able to grow well and showed good proliferation in all groups (Fig. S6C). Taken together, these results showed that the GelMA/gelatin/PEG/MSNs scaffold exhibited satisfactory biocompatibility.

3.4. Macrophage polarization of RAW264.7 cells in the 3D-bioprinted scaffolds

In patients with DM, inflammatory responses are dysregulated; for example, the ratio of M2/M1 type macrophages is decreased, which affects osteogenesis [32,33]. The increased number of M1 macrophages secrete a large number of pro-inflammatory factors, thereby altering the pro-inflammation reaction and further inhibiting osteogenesis [31,32,34,35]. For example, TNF-α, IL-1β, and IL-6 inhibit BMSCs and osteoblast proliferation and osteogenic differentiation, promote osteoblast apoptosis, and activate osteoclasts. Lipopolysaccharide and TNF-α stimulate osteoblasts to secrete receptor activator of nuclear factor κB (NF-κB) ligand, which binds to monocyte macrophage membrane receptors and promotes the differentiation of monocyte macrophages to osteoclasts by activating the NF-κB pathway. During this process, elimination of free radicals is difficult, and increased reactive oxygen species (ROS) are observed, further amplifying the inflammatory cascade. Importantly, ROS can inhibit the osteogenic differentiation of BMSCs [31,32,34–36]. In contrast, M2 type macrophages are gradually consumed in the inflammatory body, disrupting self-regulating repair of inflammation-induced damage [33]. The anti-inflammatory response of M2 type macrophages, which involves secretion of anti-inflammatory cytokines, is eliminated, and the secretion of BMP-2 by M2 type
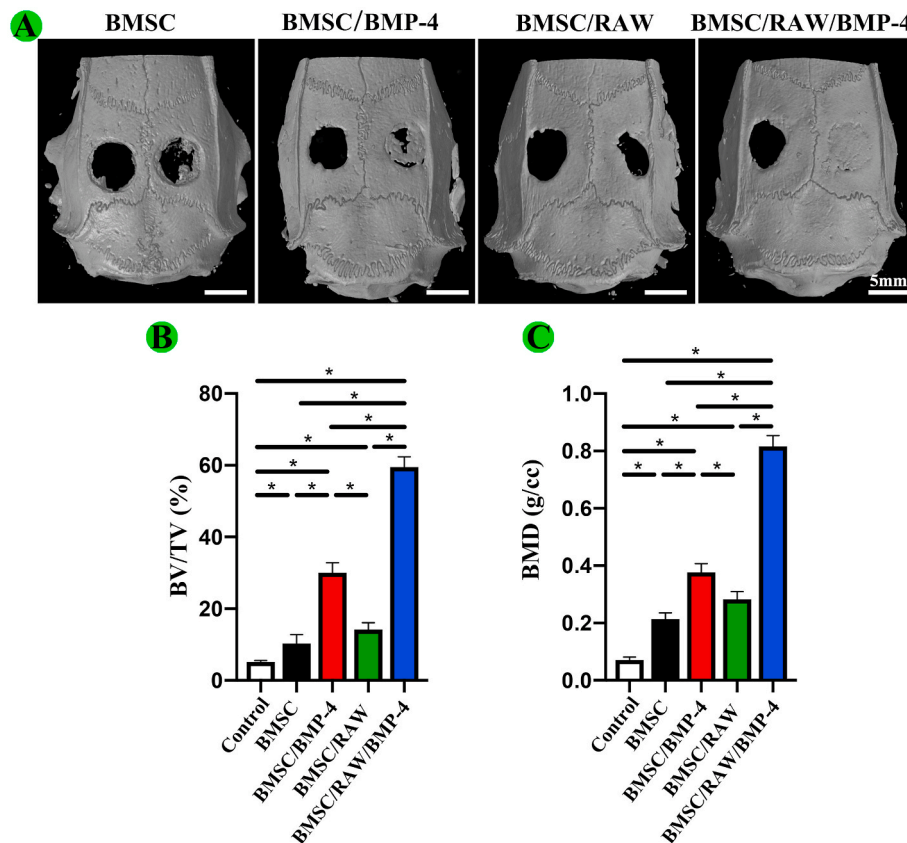
Fig. 5. Osteogenic roles of different groups in vivo. (A) 3D reconstruction of micro-CT images. The scaffolds were implanted in the right side. (B–C) Quantitative analysis of micro-CT images, including BV/TV and BMD (*$P < 0.05$).

macrophages is also reduced, further inhibiting the osteogenic differentiation of BMSCs [31]. Therefore, the decreased ratio of M2/M1 type macrophages could lead to changes in the quality and structure of the bone. These alterations could further inhibit new bone formation, affect bone reconstruction, and cause failure of bone defect repair processes.

BMP-4 directly induces the osteogenic differentiation of BMSCs by activating the Smad signaling pathway [38]. Recently, many studies have reported that BMPs induce the polarization of M2 type macrophages [41,42,57,58]. Lee et al. [57] reported that BMP-6 secreted by renal cancer cells can bind to BMPR-II on macrophages and then phosphorylate Smad5 in target cells. After phosphorylated Smad5 enters the nucleus, it physically binds to phosphorylated signal transducer and activator of transcription and then to single nucleotide polymorphisms in the promoter region of the *IL-10* gene, promoting the transcription and expression of IL-10 and further enhancing macrophage polarization to the M2 type. Moreover, BMP-4 and BMP-7 also activate the Smad signaling pathway to induce the transcription and expression of IL-10 [41,58]. Therefore, in our study, we used BMP-4 as a loading factor for 3D bioprinting and evaluated the roles of BMP-4 in M2 type polarization.

First, we performed fluorescence staining in vitro to evaluate the expression of M1 (CCR7) and M2 (CD206) markers in RAW264.7 macrophages in the RAW and RAW/BMP-4 groups. As shown in Fig. 2A and 2B, at 2 days, the fluorescence intensity of CCR7 was significantly decreased in the RAW/BMP-4 group compared with that in the RAW group ($P < 0.05$). In contrast, the fluorescence intensity of CD206 was significantly higher in the RAW/BMP-4 group than in the RAW group ($P < 0.05$). Furthermore, after 5 days culture, the fluorescence intensity of CCR7 was also significantly decreased in the RAW/BMP-4 group compared with that in the RAW group ($P < 0.05$). By contrast, the fluorescence intensity of CD206 was significantly higher in the RAW/BMP-4 group than in the RAW group ($P < 0.05$) (Fig. 2C and

2D). With the culture time prolonging, the fluorescence intensity of CD206 was also significantly increased in the RAW/BMP-4 groups. These findings indicated that BMP-4 could induce M2 type macrophage polarization.

In vivo, we implanted scaffolds from the RAW and RAW/BMP-4 groups into the calvarial defects of DM rats and performed immunohistochemical staining for detection of CCR7 and CD206 to evaluate macrophage polarization at 3 days after operation. The results also showed that BMP-4 could induce M2 type macrophage polarization (Fig. 4A and 4B).

Furthermore, we performed qRT-PCR to evaluate the gene expression of key inflammatory cytokines in the RAW and RAW/BMP-4 groups in vitro. As shown in Fig. 2E and 2F, compared with the RAW group, genes encoding pro-inflammatory cytokines, including IL-1β, IL-6, and TNF-α, were significantly downregulated in the RAW/BMP-4 group ($P < 0.05$). In contrast, genes encoding anti-inflammatory cytokines, including IL-1Rα, IL-4, and IL-10, were significantly upregulated in the RAW/BMP-4 group ($P < 0.05$).

In vivo, we performed immunohistochemical staining for detection of IL-1β and IL-10. The results also showed that BMP-4 could reduce the expression of IL-1β and increase the expression of IL-10 (Fig. 4C and 4D). Thus, these results showed that BMP-4 could induce M2 type polarization in macrophages, further inhibiting the inflammatory reaction.

3.5. Osteogenic differentiation of BMSCs in the 3D-bioprinted scaffolds

M2 type macrophages provide an anti-inflammatory microenvironment to facilitate tissue healing and produce BMP-2 improve the osteogenesis potential of BMSCs [32,37,59,60]. BMP-2 can upregulate ALP, osteocalcin, and OPN through the Smad signaling pathway, thereby promoting the osteogenic differentiation of BMSCs and
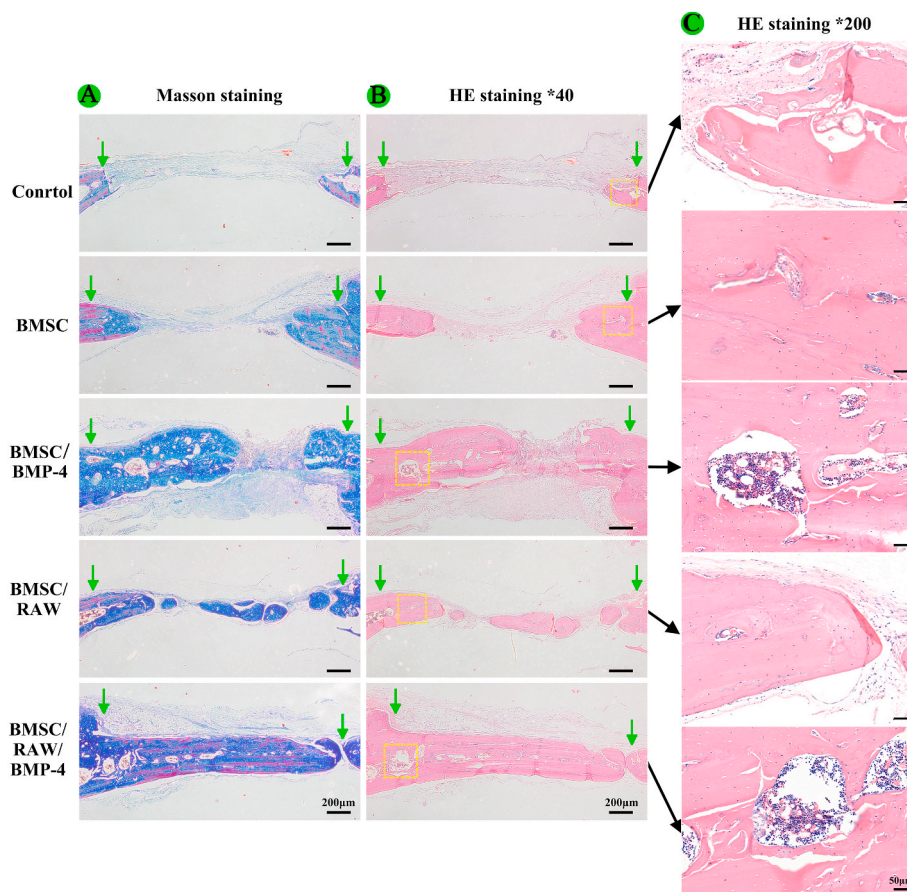
Fig. 6. HE and Masson staining of different groups in vivo. (A) Masson staining. (B) HE staining. (C) Neovascularization in bone defects (the arrow indicates the border of the bone defect).

osteoblasts [61]. In our study, we found that the expression of BMP-2 was significantly increased in the RAW/BMP-4 group compared with that in the RAW group, indicating that M2 type macrophages activated by BMP-4 could secrete BMP-2 (Fig. 2G and 2H).

To further evaluate the osteogenic effects of the different groups, we performed immunofluorescence staining for Runx2, OPN, and ALP and Alizarin red staining at different times in vitro. As shown in Fig. 3A, B, D, and E, Runx2 and OPN expression levels were the highest in BMSCs in the BMSC/BMP-4/RAW group ($P < 0.05$), followed by those in the BMSC/BMP-4 and BMSC/RAW groups. As shown in Fig. 3C and 3F, the results of ALP staining also showed that the highest expression of ALP was observed in the BMSC/RAW/BMP-4 group ($P < 0.05$). To further study the mineralization level of BMSCs in different scaffolds, we conducted Alizarin red staining at 21 days. More calcified nodules were stained red in the BMSC/BMP-4/RAW group than in the other three groups ($P < 0.05$; Fig. 3C), and the trend was further confirmed by quantitative analysis (Fig. 3G).

In our in vivo study, we established 5 mm calvarial critical-size defect models in DM rats (Fig. S7.) After 2 months of implantation, micro-CT was used to observe the new bone formation and quantitatively analyze the micro-CT data. The results confirmed that the indexes reflected new bone formation (Fig. 5A–C). We found that the BV/TV of BMSC/RAW/BMP-4 group was $59.48 \pm 0.89\%$ at 8 weeks postoperatively, which was 2.0-fold times, 4.2-fold times and 5.8-fold times higher than that of BMSC/BMP-4, BMSC/RAW, and BMSC groups. Also, the BMD result revealed the same tendency. Notably, the newly formed bone was greatest in the BMSC/RAW/BMP-4 group, indicating the better bone regeneration performance.

Furthermore, we performed HE staining and Masson staining to observe new bone growth in the calvarial region (Fig. 6). Both new

bone formation and neovascularization were observed at the bone defect region in the BMSC/RAW/BMP-4, BMSC/BMP-4, BMSC/RAW, and BMSC groups. The new bone volume and degree of neovascularization were higher in the BMSC/RAW/BMP-4 group than in the other groups.

Taken together, these results showed that the scaffolds in the BMSC/RAW/BMP-4 group showed the best osteogenic properties, followed by those in the BMSC/BMP-4 group. These findings confirmed that BMP-4 directly induced the osteogenic differentiation of BMSCs and promoted M2 type macrophage polarization, which could enhance osteogenesis.

There were some limitations to this study. Primarily, the effects of BMP-4 on polarization and osteogenesis and the ability of polarized macrophages to promote osteogenesis were not explored in sufficient detail. Indeed, further studies are needed to evaluate these mechanisms. Additionally, the previous studies suggested that BMSCs could improve the M2 type polarization and further reduced the inflammatory responses [62,63]. However, the aim of our study was to study the roles of BMP-4 to regulate macrophage polarization and inflammatory responses, and further clarified the function of M2 type macrophage to promote BMSCs osteogenesis. Therefore, for avoiding the effect of BMSCs on macrophage polarization, and clarifying the roles of BMP-4, we only designed the RAW group and RAW/BMP-4 groups in Fig. 2 and 4.

4. Conclusion

In summary, the prepared GelMA/gelatin/PEG/MSNs composite bioinks showed satisfactory printability, mechanical stability, and biocompatibility. In 3D-bioprinted scaffolds loaded with BMSCs and RAW264.7 macrophages, the sustained release of BMP-4 from MSNs induced M2 type macrophage polarization and thereby inhibited

inflammatory reactions. In addition, loading of BMP-4 and secretion of BMP-2 by M2 type macrophages promoted the osteogenic differentiation of BMSCs and further accelerated bone repair in DM bone defects. This may represent an effective method for management of bone defects in patients with DM.

Funding

CRediT authorship contribution statement

Xin Sun: Conceptualization, Methodology, Validation, Formal analysis, Investigation, Writing - original draft, Writing - review & editing, Visualization, Funding acquisition. **Zhenjiang Ma:** Conceptualization, Methodology, Formal analysis, Writing - original draft, Writing - review & editing. **Xue Zhao:** Conceptualization, Methodology, Formal analysis, Writing - original draft, Writing - review & editing. **Wenjie Jin:** Conceptualization, Formal analysis, Writing - original draft, Writing - review & editing, Visualization. **Chenyu Zhang:** Formal analysis, Writing - original draft, Writing - review & editing, Visualization. **Jie Ma:** Formal analysis, Writing - original draft, Writing - review & editing, Visualization. **Lei Qiang:** Formal analysis, Writing - original draft, Writing - review & editing, Visualization. **Wenhao Wang:** Formal analysis, Data curation, Writing - original draft, Writing - review & editing, Visualization. **Qian Deng:** Formal analysis, Writing - original draft, Writing - review & editing, Visualization. **Han Yang:** Formal analysis, Writing - original draft, Visualization. **Jinzhong Zhao:** Methodology, Writing - original draft, Visualization. **Qianqian Liang:** Methodology, Writing - original draft, Visualization. **Xiaojun Zhou:** Conceptualization, Methodology, Validation, Investigation, Writing - original draft, Writing - review & editing, Visualization, Supervision, Funding acquisition. **Tao Li:** Conceptualization, Methodology, Validation, Investigation, Writing - original draft, Writing - review & editing, Supervision, Funding acquisition. **Jinwu Wang:** Conceptualization, Methodology, Validation, Investigation, Writing - original draft, Writing - review & editing, Supervision, Project administration, Funding acquisition.

Declaration of competing interest

There are no any interest conflicts.

Acknowledgment

The authors would like to thank Dr. Ling Qin of the Chinese University of Hong Kong for his advice on improving the manuscript.

Appendix A. Supplementary data

Supplementary data to this article can be found online at https://doi.org/10.1016/j.bioactmat.2020.08.030.

References

[1] L. Guariguata, D.R. Whiting, I. Hambleton, J. Beagley, U. Linnenkamp, J.E. Shaw, Global estimates of diabetes prevalence for 2013 and projections for 2035, Diabetes Res. Clin. Pract. 103 (2014) 137–149, https://doi.org/10.1016/j.diabres.2013.11.002.
[2] A.D. Dede, S. Tournis, I. Dontas, G. Trovas, Type 2 diabetes mellitus and fracture risk, Metabolism 63 (2014) 1480–1490, https://doi.org/10.1016/j.metabol.2014.09.002.
[3] H. Jiao, E. Xiao, D.T. Graves, Diabetes and its effect on bone and fracture healing, Curr. Osteoporos. Rep. 13 (2015) 327–335, https://doi.org/10.1007/s11914-015-0286-8.
[4] N. Shibuya, J.M. Humphers, B.L. Fluhman, D.C. Jupiter, Factors associated with nonunion, delayed union, and malunion in foot and ankle surgery in diabetic patients, J. Foot Ankle Surg. 52 (2013) 207–211, https://doi.org/10.1053/j.jfas.2012.11.012.
[5] M.N. Hassan, M.A. Yassin, S. Suliman, S.A. Lie, H. Gjengedal, K. Mustafa, The bone regeneration capacity of 3D-printed templates in calvarial defect models: a systematic review and meta-analysis, Acta Biomater. 91 (2019) 1–23, https://doi.org/10.1016/j.actbio.2019.04.017.
[6] Y. Lai, Y. Li, H. Cao, J. Long, X. Wang, L. Li, C. Li, Q. Jia, B. Teng, T. Tang, J. Peng, D. Eglin, M. Alini, D.W. Grijpma, G. Richards, L. Qin, Osteogenic magnesium incorporated into PLGA/TCP porous scaffold by 3D printing for repairing challenging bone defect, Biomaterials 197 (2019) 207–219, https://doi.org/10.1016/j.biomaterials.2019.01.013.
[7] J.J. Li, C.R. Dunstan, A. Entezari, Q. Li, R. Steck, S. Saifzadeh, A. Sadeghpour, J.R. Field, A. Akey, M. Vielreicher, O. Friedrich, S.I. Roohani-Esfahani, H. Zreiqat, A novel bone substitute with high bioactivity, strength, and porosity for repairing large and load-bearing bone defects, Adv Healthc Mater 8 (2019) e1801298, , https://doi.org/10.1002/adhm.201801298.
[8] C. Hamann, C. Goettsch, J. Mettelsiefen, V. Henkenjohann, M. Rauner, U. Hempel, R. Bernhardt, N. Fratzl-Zelman, P. Roschger, S. Rammelt, K.P. Gunther, L.C. Hofbauer, Delayed bone regeneration and low bone mass in a rat model of insulin-resistant type 2 diabetes mellitus is due to impaired osteoblast function, Am. J. Physiol. Endocrinol. Metab. 301 (2011) E1220–E1228, https://doi.org/10.1152/ajpendo.00378.2011.
[9] N. Ashammakhi, A. Hasan, O. Kaarela, B. Byambaa, A. Sheikhi, A.K. Gaharwar, A. Khademhosseini, Advancing frontiers in bone bioprinting, Adv Healthc Mater 8 (2019) e1801048, , https://doi.org/10.1002/adhm.201801048.
[10] H.W. Kang, S.J. Lee, I.K. Ko, C. Kengla, J.J. Yoo, A. Atala, A 3D bioprinting system to produce human-scale tissue constructs with structural integrity, Nat. Biotechnol. 34 (2016) 312–319, https://doi.org/10.1038/nbt.3413.
[11] Z.Z. Zhang, Y.R. Chen, S.J. Wang, F. Zhao, X.G. Wang, F. Yang, J.J. Shi, Z.G. Ge, W.Y. Ding, Y.C. Yang, T.Q. Zou, J.Y. Zhang, J.K. Yu, D. Jiang, Orchestrated biomechanical, structural, and biochemical stimuli for engineering anisotropic meniscus, Sci. Transl. Med. 11 (2019), https://doi.org/10.1126/scitranslmed.aao0750.
[12] X. Zhai, C. Ruan, Y. Ma, D. Cheng, M. Wu, W. Liu, X. Zhao, H. Pan, W.W. Lu, 3D-Bioprinted osteoblast-laden nanocomposite hydrogel constructs with induced microenvironments promote cell viability, differentiation, and osteogenesis both in vitro and in vivo, Adv. Sci. 5 (2018) 1700550, https://doi.org/10.1002/advs.201700550.
[13] G. Cidonio, M. Glinka, J.I. Dawson, R.O.C. Oreffo, The cell in the ink: improving biofabrication by printing stem cells for skeletal regenerative medicine, Biomaterials 209 (2019) 10–24, https://doi.org/10.1016/j.biomaterials.2019.04.009.
[14] T.T. Demirtas, G. Irmak, M. Gumusderelioglu, A bioprintable form of chitosan hydrogel for bone tissue engineering, Biofabrication 9 (2017) 035003, , https://doi.org/10.1088/1758-5090/aa7b1d.
[15] P.S. Gungor-Ozkerim, I. Inci, Y.S. Zhang, A. Khademhosseini, M.R. Dokmeci, Bioinks for 3D bioprinting: an overview, Biomater Sci 6 (2018) 915–946, https://doi.org/10.1039/c7bm00765e.
[16] J. Yin, M. Yan, Y. Wang, J. Fu, H. Suo, 3D bioprinting of low-concentration cell-laden gelatin methacrylate (GelMA) bioinks with a two-step cross-linking strategy, ACS Appl. Mater. Interfaces 10 (2018) 6849–6857, https://doi.org/10.1021/acsami.7b16059.
[17] H. Stratesteffen, M. Kopf, F. Kreimendahl, A. Blaeser, S. Jockenhoevel, H. Fischer, GelMA-collagen blends enable drop-on-demand 3D printablility and promote angiogenesis, Biofabrication 9 (2017) 045002, , https://doi.org/10.1088/1758-5090/aa857c.
[18] C. McBeth, J. Lauer, M. Ottersbach, J. Campbell, A. Sharon, A.F. Sauer-Budge, 3D bioprinting of GelMA scaffolds triggers mineral deposition by primary human osteoblasts, Biofabrication 9 (2017) 015009, , https://doi.org/10.1088/1758-5090/aa53bd.
[19] K. Holzl, S. Lin, L. Tytgat, S. Van Vlierberghe, L. Gu, A. Ovsianikov, Bioink properties before, during and after 3D bioprinting, Biofabrication 8 (2016) 032002, , https://doi.org/10.1088/1758-5090/8/3/032002.
[20] C. Colosi, S.R. Shin, V. Manoharan, S. Massa, M. Costantini, A. Barbetta, M.R. Dokmeci, M. Dentini, A. Khademhosseini, Microfluidic bioprinting of heterogeneous 3D tissue constructs using low-viscosity bioink, Adv Mater 28 (2016) 677–684, https://doi.org/10.1002/adma.201503310.
[21] T. Billiet, E. Gevaert, T. De Schryver, M. Cornelissen, P. Dubruel, The 3D printing of gelatin methacrylamide cell-laden tissue-engineered constructs with high cell viability, Biomaterials 35 (2014) 49–62, https://doi.org/10.1016/j.biomaterials.2013.09.078.

[22] A. Garcia-Lizarribar, X. Fernandez-Garibay, F. Velasco-Mallorqui, A.G. Castano, J. Samitier, J. Ramon-Azcon, Composite biomaterials as long-lasting scaffolds for 3D bioprinting of highly aligned muscle tissue, Macromol. Biosci. 18 (2018) e1800167, , https://doi.org/10.1002/mabi.201800167.

[23] Q. Gao, X. Niu, L. Shao, L. Zhou, Z. Lin, A. Sun, J. Fu, Z. Chen, J. Hu, Y. Liu, Y. He, 3D printing of complex GelMA-based scaffolds with nanoclay, Biofabrication 11 (2019) 035006, , https://doi.org/10.1088/1758-5090/ab0cf6.

[24] A. Wubneh, E.K. Tsekoura, C. Ayranci, H. Uludag, Current state of fabrication technologies and materials for bone tissue engineering, Acta Biomater. 80 (2018) 1–30, https://doi.org/10.1016/j.actbio.2018.09.031.

[25] Z. Wang, R. Abdulla, B. Parker, R. Samanipour, S. Ghosh, K. Kim, A simple and high-resolution stereolithography-based 3D bioprinting system using visible light crosslinkable bioinks, Biofabrication 7 (2015) 045009, , https://doi.org/10.1088/1758-5090/7/4/045009.

[26] S.J. Bryant, R.J. Bender, K.L. Durand, K.S. Anseth, Encapsulating chondrocytes in degrading PEG hydrogels with high modulus: engineering gel structural changes to facilitate cartilaginous tissue production, Biotechnol. Bioeng. 86 (2004) 747–755, https://doi.org/10.1002/bit.20160.

[27] A.S. Qayyum, E. Jain, G. Kolar, Y. Kim, S.A. Sell, S.P. Zustiak, Design of electro-hydrodynamic sprayed polyethylene glycol hydrogel microspheres for cell encapsulation, Biofabrication 9 (2017) 025019, , https://doi.org/10.1088/1758-5090/aa703c.

[28] N. Esser, S. Legrand-Poels, J. Piette, A.J. Scheen, N. Paquot, Inflammation as a link between obesity, metabolic syndrome and type 2 diabetes, Diabetes Res. Clin. Pract. 105 (2014) 141–150, https://doi.org/10.1016/j.diabres.2014.04.006.

[29] A.K. Picke, J. Salbach-Hirsch, V. Hintze, S. Rother, M. Rauner, C. Kascholke, S. Moller, R. Bernhardt, S. Rammelt, M.T. Pisabarro, G. Ruiz-Gomez, M. Schnabelrauch, M. Schulz-Siegmund, M.C. Hacker, D. Scharnweber, C. Hofbauer, L.C. Hofbauer, Sulfated hyaluronan improves bone regeneration of diabetic rats by binding sclerostin and enhancing osteoblast function, Biomaterials 96 (2016) 11–23, https://doi.org/10.1016/j.biomaterials.2016.04.013.

[30] Z. Hu, C. Ma, X. Rong, S. Zou, X. Liu, Immunomodulatory ECM-like microspheres for accelerated bone regeneration in diabetes mellitus, ACS Appl. Mater. Interfaces 10 (2018) 2377–2390, https://doi.org/10.1021/acsami.7b18458.

[31] Z. Jamalpoor, A. Asgari, M.H. Lashkari, A. Mirshafiey, M. Mohsenzadegan, Modulation of macrophage polarization for bone tissue engineering applications, Iran. J. Allergy, Asthma Immunol. 17 (2018) 398–408.

[32] N.J. Horwood, Macrophage polarization and bone formation: a review, Clin. Rev. Allergy Immunol. 51 (2016) 79–86, https://doi.org/10.1007/s12016-015-8519-2.

[33] C.Y. Wang, H.B. Yang, H.S. Hsu, L.L. Chen, C.C. Tsai, K.S. Tsai, T.L. Yew, Y.H. Kao, S.C. Hung, Mesenchymal stem cell-conditioned medium facilitates angiogenesis and fracture healing in diabetic rats, J Tissue Eng Regen Med 6 (2012) 559–569, https://doi.org/10.1002/term.461.

[34] K.I. Ko, L.S. Coimbra, C. Tian, J. Alblowi, R.A. Kayal, T.A. Einhorn, L.C. Gerstenfeld, R.J. Pignolo, D.T. Graves, Diabetes reduces mesenchymal stem cells in fracture healing through a TNFalpha-mediated mechanism, Diabetologia 58 (2015) 633–642, https://doi.org/10.1007/s00125-014-3470-y.

[35] G.P. Fadini, S.V. de Kreutzenberg, E. Boscaro, M. Albiero, R. Cappellari, N. Krankel, U. Landmesser, A. Toniolo, C. Bolego, A. Cignarella, F. Seeger, S. Dimmeler, A. Zeiher, C. Agostini, A. Avogaro, An unbalanced monocyte polarisation in peripheral blood and bone marrow of patients with type 2 diabetes has an impact on microangiopathy, Diabetologia 56 (2013) 1856–1866, https://doi.org/10.1007/s00125-013-2918-9.

[36] O. Kose, T. Arabaci, A. Kara, H. Yemenoglu, E. Kermen, A. Kizildag, S. Gedikli, S. Ozkanlar, Effects of melatonin on oxidative stress index and alveolar bone loss in diabetic rats with periodontitis, J. Periodontol. 87 (2016) e82–90, https://doi.org/10.1902/jop.2016.150541.

[37] Y. Wang, W. Smith, D. Hao, B. He, L. Kong, M1 and M2 macrophage polarization and potentially therapeutic naturally occurring compounds, Int. Immunopharm. 70 (2019) 459–466, https://doi.org/10.1016/j.intimp.2019.02.050.

[38] V.S. Salazar, L.W. Gamer, V. Rosen, BMP signalling in skeletal development, disease and repair, Nat. Rev. Endocrinol. 12 (2016) 203–221, https://doi.org/10.1038/nrendo.2016.12.

[39] B.S. Yurekli, G.U. Kocabas, M. Aksit, N.O. Kutbay, A. Suner, I. Yurekli, H. Cakir, G. Bozkaya, S. Cetinkalp, The low levels of bone morphogenic protein-4 and its antagonist noggin in type 2 diabetes, Hormones (Basel) 17 (2018) 247–253, https://doi.org/10.1007/s42000-018-0041-5.

[40] M. Retzepi, E. Calciolari, I. Wall, M.P. Lewis, N. Donos, The effect of experimental diabetes and glycaemic control on guided bone regeneration: histology and gene expression analyses, Clin. Oral Implants Res. 29 (2018) 139–154, https://doi.org/10.1111/clr.13031.

[41] V.G. Martinez, C. Rubio, M. Martinez-Fernandez, C. Segovia, F. Lopez-Calderon, M.I. Garin, A. Teijeira, E. Munera-Maravilla, A. Varas, R. Sacedon, F. Guerrero, F. Villacampa, F. de la Rosa, D. Castellano, E. Lopez-Collazo, J.M. Paramio, A. Vicente, N. Duenas, BMP4 induces M2 macrophage polarization and favors tumor progression in bladder cancer, Clin. Canc. Res. 23 (2017) 7388–7399, https://doi.org/10.1158/1078-0432.ccr-17-1004.

[42] J. Valencia, L. MF-S, A. Fraile-Ramos, R. Sacedon, E. Jimenez, A. Vicente, A. Varas, Acute lymphoblastic leukaemia cells impair dendritic cell and macrophage differentiation: role of BMP4, Cells (2019) 8, https://doi.org/10.3390/cells8070722.

[43] Y. Shiozaki, T. Kitajima, T. Mazaki, A. Yoshida, M. Tanaka, A. Umezawa, M. Nakamura, Y. Yoshida, Y. Ito, T. Ozaki, A. Matsukawa, Enhanced in vivo osteogenesis by nanocarrier-fused bone morphogenetic protein-4, Int. J. Nanomed. 8

(2013) 1349–1360, https://doi.org/10.2147/ijn.s44124.

[44] Yutian, Z. Li, W. Zhang, Y. Li, Y. Yuan, C. Liu, Size-Mediated adsorption dynamics, conformation and bioactivity of bone morphogenetic protein-2 onto silica nanoparticles, J. Nanosci. Nanotechnol. 16 (2016) 5528–5536, https://doi.org/10.1166/jnn.2016.11743.

[45] Q. Yao, Q. Liu, B. Selvaratnam, R.T. Koodali, H. Sun, Mesoporous silicate nanoparticles/3D nanofibrous scaffold-mediated dual-drug delivery for bone tissue engineering, J. Contr. Release 279 (2018) 69–78, https://doi.org/10.1016/j.jconrel.2018.04.011.

[46] C. Mahapatra, R.K. Singh, J.J. Kim, K.D. Patel, R.A. Perez, J.H. Jang, H.W. Kim, Osteopromoting reservoir of stem cells: bioactive mesoporous nanocarrier/collagen gel through slow-releasing FGF18 and the activated BMP signaling, ACS Appl. Mater. Interfaces 8 (2016) 27573–27584, https://doi.org/10.1021/acsami.6b09769.

[47] S.R.U. Rehman, R. Augustine, A.A. Zahid, R. Ahmed, M. Tariq, A. Hasan, Reduced graphene oxide incorporated GelMA hydrogel promotes angiogenesis for wound healing applications, Int. J. Nanomed. 14 (2019) 9603–9617, https://doi.org/10.2147/ijn.s218120.

[48] A.R. Spencer, E. Shirzaei Sani, J.R. Soucy, C.C. Corbet, A. Primbetova, R.A. Koppes, N. Annabi, Bioprinting of a cell-laden conductive hydrogel composite, ACS Appl. Mater. Interfaces 11 (2019) 30518–30533, https://doi.org/10.1021/acsami.9b07353.

[49] X. Xu, K. Fang, L. Wang, X. Liu, Y. Zhou, Y. Song, Local application of semaphorin 3A combined with adipose-derived stem cell sheet and anorganic bovine bone granules enhances bone regeneration in type 2 diabetes mellitus rats, Stem Cell. Int. 2019 (2019) 2506463, https://doi.org/10.1155/2019/2506463.

[50] S.F. Durao, P.S. Gomes, B.J. Colaco, J.C. Silva, H.M. Fonseca, J.R. Duarte, A.C. Felino, M.H. Fernandes, The biomaterial-mediated healing of critical size bone defects in the ovariectomized rat, Osteoporos. Int. 25 (2014) 1535–1545, https://doi.org/10.1007/s00198-014-2656-y.

[51] X. Sun, Z. Wu, D. He, K. Shen, X. Liu, H. Li, W. Jin, Bioactive injectable polymethylmethacrylate/silicate bioceramic hybrid cements for percutaneous vertebroplasty and kyphoplasty, J Mech Behav Biomed Mater 96 (2019) 125–135, https://doi.org/10.1016/j.jmbbm.2019.04.044.

[52] T. Li, M. Peng, Z. Yang, X. Zhou, Y. Deng, C. Jiang, M. Xiao, J. Wang, 3D-printed IFN-gamma-loading calcium silicate-beta-tricalcium phosphate scaffold sequentially activates M1 and M2 polarization of macrophages to promote vascularization of tissue engineering bone, Acta Biomater. 71 (2018) 96–107, https://doi.org/10.1016/j.actbio.2018.03.012.

[53] X. Zhou, W. Weng, B. Chen, W. Feng, W. Wang, W. Nie, L. Chen, X. Mo, J. Su, C. He, Mesoporous silica nanoparticles/gelatin porous composite scaffolds with localized and sustained release of vancomycin for treatment of infected bone defects, J. Mater. Chem. B 6 (2018) 740–752, https://doi.org/10.1039/c7tb01246b.

[54] J. Pan, J. Deng, L. Yu, Y. Wang, W. Zhang, X. Han, P.H.C. Camargo, J. Wang, Y. Liu, Investigating the repair of alveolar bone defects by gelatin methacrylate hydrogels-encapsulated human periodontal ligament stem cells, J. Mater. Sci. Mater. Med. 31 (2019) 3, https://doi.org/10.1007/s10856-019-6333-8.

[55] K. Yue, G. Trujillo-de Santiago, M.M. Alvarez, A. Tamayol, N. Annabi, A. Khademhosseini, Synthesis, properties, and biomedical applications of gelatin methacryloyl (GelMA) hydrogels, Biomaterials 73 (2015) 254–271, https://doi.org/10.1016/j.biomaterials.2015.08.045.

[56] J. Sammons, N. Ahmed, M. El-Sheemy, H.T. Hassan, The role of BMP-6, IL-6, and BMP-4 in mesenchymal stem cell-dependent bone development: effects on osteoblastic differentiation induced by parathyroid hormone and vitamin D(3), Stem Cell. Dev. 13 (2004) 273–280, https://doi.org/10.1089/154732804323099208.

[57] J.H. Lee, G.T. Lee, S.H. Woo, Y.S. Ha, S.J. Kwon, W.J. Kim, I.Y. Kim, BMP-6 in renal cell carcinoma promotes tumor proliferation through IL-10-dependent M2 polarization of tumor-associated macrophages, Cancer Res 73 (2013) 3604–3614, https://doi.org/10.1158/0008-5472.can-12-4563.

[58] C. Rocher, D.K. Singla, SMAD-PI3K-Akt-mTOR pathway mediates BMP-7 polarization of monocytes into M2 macrophages, PloS One 8 (2013) e84009, , https://doi.org/10.1371/journal.pone.0084009.

[59] N. Wang, J. Gao, M. Jia, X. Ma, Z. Lei, F. Da, F. Yan, H. Zhang, Y. Zhou, M. Li, G. He, J. Meng, X. Luo, Exendin-4 induces bone marrow stromal cells migration through bone marrow-derived macrophages polarization via PKA-STAT3 signaling pathway, Cell. Physiol. Biochem. 44 (2017) 1696–1714, https://doi.org/10.1159/000485776.

[60] M. Du, B. Chen, Q. Meng, S. Liu, X. Zheng, C. Zhang, H. Wang, H. Li, N. Wang, J. Dai, 3D bioprinting of BMSC-laden methacrylamide gelatin scaffolds with CBD-BMP2-collagen microfibers, Biofabrication 7 (2015) 044104, , https://doi.org/10.1088/1758-5090/7/4/044104.

[61] B. Poon, T. Kha, S. Tran, C.R. Dass, Bone morphogenetic protein-2 and bone therapy: successes and pitfalls, J. Pharm. Pharmacol. 68 (2016) 139–147, https://doi.org/10.1111/jphp.12506.

[62] T. Li, Z.L. Liu, M. Xiao, Z.Z. Yang, M.Z. Peng, C.D. Li, X.J. Zhou, J.W. Wang, Impact of bone marrow mesenchymal stem cell immunomodulation on the osteogenic effects of laponite, Stem Cell Res. Ther. 9 (2018) 100, https://doi.org/10.1186/s13287-018-0818-0.

[63] Y.H. Zheng, Y.Y. Deng, W. Lai, S.Y. Zheng, H.N. Bian, Z.A. Liu, Z.F. Huang, C.W. Sun, H.H. Li, H.M. Luo, L.H. Ma, H.X. Chen, B. Xiong, Effect of bone marrow mesenchymal stem cells on the polarization of macrophages, Mol. Med. Rep. 17 (2018) 4449–4459, https://doi.org/10.3892/mmr.2018.8457.